# Micro-scratching behavior of heat-treated cutting chips of Inconel 718

Prabhat Chand Yadav[1, a, *], Prince Setia[2, b], Sandeep Sahu[3, 4, c]
[1]Department of Mechanical Engineering, Thapar Institute of Engineering & Technology, Patiala - 147004, India
[2]Department of Materials Science and Engineering, Indian Institute of Technology Kanpur, Kanpur - 208016, India
[3]Directorate of Nanomaterials, Defence Materials and Stores Research and Development Establishment, Kanpur - 208013, India
[4]Department of Mechanical Engineering, University of Southampton, Highfield Campus, Southampton- SO17 1BJ, United Kingdom

[a]prabhatchand.yadav@thapar.edu, [b]psetia@iitk.ac.in, [c]s.sahu@soton.ac.uk

*Corresponding authors

## Abstract

The present work investigates the wear behavior of Inconel 718 alloy processed by machining and subsequent heat-treatment. As-machined chips were heat-treated at 700 °C, 800 °C, and 900 °C, all for a short duration of 15 min, followed by water quenching to allow the precipitation of $\gamma^{/}$ and $\gamma^{//}$ phases. Microstructural analysis of the processed Inconel 718 chips revealed the formation of nano-size precipitates either along the grain boundaries or at the triple junctions, which contributed to the improved mechanical property compared to the solution annealed sample. It was found that the chips heat-treated at 700 °C possessed the highest average hardness (548 Kgf/mm$^2$) among all the sample conditions. High hardness of as-machined chips and short heat-treatment at 700 °C led bimodal microstructure and precipitation pining resulting in maximum wear resistance compared to other heat-treatment conditions. Subsequently, to verify the outcome, worn surface analysis of as-machined and subsequently heat-treated chips was performed. Comparatively, larger size cracks in sample heat-treated at 900 °C attributed to a high cracking scratch zone in the processed material,

*Corresponding author: Dr. Prabhat Chand Yadav, BC-104, Department of Mechanical Engineering, Thapar Institute of Engineering and Technology Patiala, 147004, India.
Email ID: prabhatchand.yadav@thapar.edu

i.e., less wear resistance, whereas no/nominal crack in as-machined chips and chips heat-treated at 700 °C attributed to no cracking scratch zone.

**Keywords:** Inconel 718, Severe plastic deformation, Heat-treatment, Mechanical property, Wear behavior, Scratch test

## 1. Introduction

Inconel 718 (IN718) is a Ni-Cr-Fe-based austenitic precipitation-hardenable superalloy with good strength (e.g., yield strength ~ 447 MPa, ultimate tensile strength ~ 897, and ductility ~ 43.5% at room temperature for solution annealed condition [1]) and toughness, high resistance to oxidation and corrosion; and good machining performance [2,3]. Also, they are known to showcase better mechanical properties at elevated temperatures [4]. Moreover, they exhibit excellent resistance to creep, fatigue, wear, and chemical degradation in a high-pressure working environment and excellent weldability [5]. These properties make IN718 suitable for various crucial applications like cryogenic tankage, liquid rockets, gas turbines, turbocharger rotors, aerospace industries, oil and gas industries, and nuclear reactors [6,7]. These vital applications of IN718 make it a great interest for research and development to understand its microstructural, mechanical, and wear behavior followed by underlying micro-mechanisms behind its failure.

IN718 components are generally manufactured using casting and various metal forming processes [8]. Machining is a widely used manufacturing technique for sizing, shaping, and finishing of metallic components. However, IN718 is tremendously hard to machine owing to several plastic deformations caused by machining on the machined surface. The primary reasons for this are high strength and toughness, high work hardening behavior, chemical affinity towards many tool materials, and poor thermal conductivity of IN718 [9,10]. Wright and Chow [11] observed that during the machining of nickel-based alloys, the normal stresses on tool faces were approximately double, and the temperatures rose 200-400 °C higher than those during the machining of steel. Such effects alter the surface and subsurface microstructure, which eventually degrades the corrosion, fatigue, and wear resistance of IN718. Therefore, it is interesting to explore and understand the micro-mechanism leading to the failure of these alloys during operation.

IN718 components rub against each other throughout various service applications, generating wear and increasing clearance in moving parts. Thus, the wear resistance of any material must be enhanced in order to improve the lifespan of components during sliding contact [12,13]. For it, the material needs to be strengthened. This can be achieved by grain refinement using severe plastic deformation (SPD) techniques. SPD processes impart a large amount of strain into the material, resulting in grain refinement and increased strength without a significant loss of ductility. Machining is a kind of SPD technique that is very effective in refining the microstructure on the machined surface and subsurface.

Over the previous years, several authors have analyzed the effect of machining on the machined surface and subsurface in IN718 [14,15]. It has been proposed that the workpiece always experiences severe plastic deformation during the metal cutting operation, leading to an improvement in the mechanical properties of the workpiece [16]. During machining of IN718, Liao et al. [17] found that grain refinement of ~200 nm sized grains occurred in a thin region ~3 to 4 μm beneath the workpiece surface. Zhuang et al. [18] experimentally analyzed the correlation between the work hardening layer and the notch wear and discovered that a critical hardened layer depth exists beneath the machined surface. Touazine et al. [19] investigated the critical hardened layer depth of work-hardened layers during multi-step hard turning (consisting of semi-finish, finish, and critical finish) of IN718 and observed it to be a maximum of 11 μm. Pawade et al. [10] assessed the effect of high-speed turning on surface integrity in IN718 and observed a machine-affected zone up to a depth of 200 μm beneath the machined surface. Ezugwu et al. [20] observed the extent of work hardening of the machined surface up to a depth of 0.6 mm. A direct relation was found between the machining parameters and the degree of work hardening during the machining of IN718 by Thakur et al. [21]. Ren and Liu [22] demonstrated that an increase in the cutting speed causes a decrease in the depth of work hardening and an increase in the degree of work hardening. Rinaldi et al. [23] found that the dynamic recrystallization and the interaction of mobile and immobile dislocations affect the microstructure of the machined surface during the machining of IN718. This is mainly attributed to grain refinement, which consequently increases the hardness of the subsurface layer. Zhou et al. [24] observed a minor difference in the hardness near the subsurface layer in the specimens machined by CBN-coated and uncoated cutting tools. Devillez et al. [25] found that the dry machining of IN718 is helpful in reducing the surface roughness.

From the preceding literature survey, it becomes clear that severe plastic deformation, such as the dry machining of direct aged IN718, affects the surface and subsurface microstructure. For their prospective uses in applications involving movable components in contact with each other, the tribological wear behavior of the machined surface needs to be investigated. Hence, in this work, we aim to investigate the wear characteristics of IN718 surface produced after plane strain machining and subsequent heat-treatments. Here, dry face turning of IN718 rod using an uncoated carbide round insert was performed. Microstructural analyses of IN718 were performed before and after the machining and subsequent heat-treatments. After the wear test, the worn surface morphology of all samples was characterized using scanning electron microscopy (SEM) and energy dispersing spectroscopy (EDS).

## 2. Material and Methods

### 2.1. Material

Precipitation-treated Nickel-based superalloy, IN718, was utilized as an initial material. The chemical composition of the as-received IN718 alloy was examined using optical emission spectroscopy (OES), and it is shown in Table 1.

Table 1: Chemical composition (wt. %) of IN718 alloy used in the machining process [3].

| Ni | Cr | Nb | Mo | Ti | Al | Mn | Si | B | C | Fe | Ta | V | W | Co |
|---|---|---|---|---|---|---|---|---|---|---|---|---|---|---|
| 54.1 | 18.54 | 4.13 | 3.12 | 0.94 | 0.49 | 0.076 | 0.18 | 0.003 | 0.056 | 17.47 | 0.181 | 0.0755 | 0.195 | 0.247 |

### 2.2. Processing

As-received samples of nickel-based superalloy (IN718) were solutionized at 1035 °C for 1 h, followed by water quenching. These samples were machined using a 0° rake angle tungsten carbide cutting tool. After processing of material using plane strain machining, the strain induced in the material was calculated. Net effective strain in severely deformed material (i.e., machined IN718 chips) was analyzed using equation $\Upsilon = \frac{\cos\alpha}{\sin\phi\cos(\alpha-\phi)}$ [26,27] where $\phi$ is the shear plane angle, and $\alpha$ is the rake angle. The equivalent strain in the chips was calculated to be ~ 1.7.

IN718 superalloy has a tendency to form various nano-precipitates like $\gamma^{/}$ and $\gamma^{//}$ in specific temperature ranges, which improve the mechanical and wear behavior of the heat-treated alloy. For this purpose, as-deformed IN718 chips were heat-treated at different temperatures — 700 °C, 800 °C, and 900 °C for 15 min, followed by water quenching to favor the formation of nano-precipitates, i.e., $\gamma^{/}$ and $\gamma^{//}$ in the FCC $\gamma$-matrix. To characterize the microstructure and test the mechanical and wear behavior, processed chips were polished using SiC emery papers followed by cloth polishing with 1 µm and 0.05 µm size alumina powder solution. For orientation imaging microscopy (OIM) analysis, an electropolishing was performed after the previous polishing steps, using Struers's Lectropol 5 with an electrolyte consisting of perchloric acid, 2-butoxyethanol, and ethanol.

The following nomenclature corresponding to different samples was adopted in the current investigation: as-received sample heat-treated at 1035 °C for 1 h is called as solution annealed (SA), as-machined chips using 0° rake angle cutting tool is AM, post-process heat-treated chips at 700 °C for 15 min is SH7, post-process heat-treated chips at 800 °C for 15 min is SH8, and post-process heat-treated chips at 900 °C for 15 min is SH9.

### 2.3. Scratch test

The wear behavior of different samples was evaluated using a micro-scratch test under dry sliding conditions at room temperature (~25 °C) in the ambient environment. Rockwell micro-indenter (CSM international, Switzerland) was pressed against the test specimen with selected normal load and moved with constant velocity, producing a scratch of a certain shape and size on the test specimen. Indenter cone material was diamond with a tip radius of 100 μm. Scratch test was performed in progressive mode from 50 mN to 5000 mN and loading rate 9900 mN/min over the scratch track length (L) of 500 μm. The schematic details of the scratch test setup used in the current study are shown in Fig. 1. During the scratch test, the difference in the indenter displacement, scratch depth, normal force, tangential force, and acoustic emission were recorded to calculate the wear-related parameters like the coefficient of friction, wear volume, and wear rate.

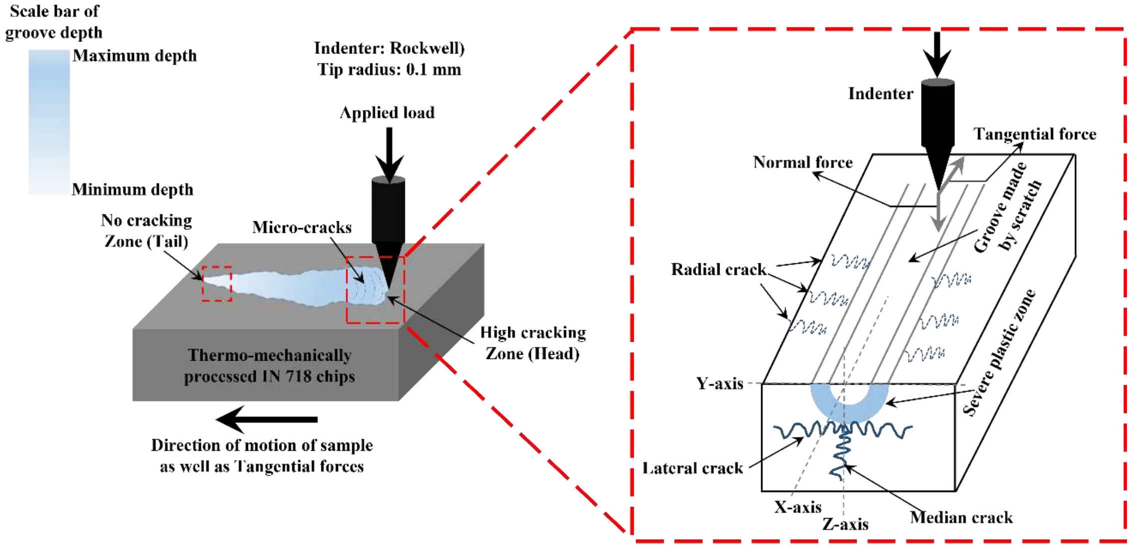

Fig. 1: Schematic of the scratch test set up for wear behavior analysis of as-machined and subsequently heat-treated IN718 alloy (adapted from Nisar et al. [28]).

Further, to investigate the overall effect of machining and post-process thermal treatment on the wear damage, wear volume (Eq. 1-2) [29] and wear rate was estimated using the Archard wear equation (Eq. 3) [29,30].

$$\text{Wear volume } (W_v) = L * A \tag{1}$$

$$A = R^2 \text{Cos}^{-1}\left(1 - \frac{p}{R}\right) - (R - p)\sqrt{2Rp - p^2} \tag{2}$$

$$\text{Sp.} W_r = \frac{W_v}{F * L} \tag{3}$$

where L is the length of scratch (mm), A is the area of the scratch region ($mm^2$), p is the depth of penetration (µm), $W_v$ is wear volume ($\mu m^3$), R is the radius of scratch at the maximum depth of penetration (µm), Sp. $W_r$ is specific wear rate ($\mu m^3$/mN.µm), F is the average normal load applied during progressive loading scratch test, which is ~2516 mN, and $W_r$ is the specific wear rate ($\mu m^3$/mN-µm) respectively.

# 3. Results and discussion

## 3.1. Microstructural evolution

### *3.1.1. Orientation Imaging Microscopy*

The samples were thoroughly investigated for microstructure analysis using the electron backscattered diffraction (EBSD) based OIM technique [31]. Fig. 2 (a-e) illustrates inverse pole figure (IPF) maps of SA, AM, and short heat-treated chips. For SA sample, the average grain size is ~28 µm, without any deformation (Fig. 2a). After machining, the banded structure containing the alternative bands of moderately refined grains and unindexed points are observed within the microstructure (Fig. 2b). The unindexed points refer to the nano-structured grains, which were produced as sheared zone during machining and could not be indexed during OIM data acquisition. Thus, the microstructure of the machined chips of IN718 (i.e., AM specimen) inherently consists of a 'bimodal' microstructure. This is known to improve the ductility of the material owing to the presence of bimodal grain size distribution. Hence, the machined chips can be expected to exhibit a combination of excellent strength and enhanced ductility. However, few studies have suggested that as-machined chips are generally brittle in nature in spite of having a bimodal grain structure, which might be due to the saturation of dislocations in nano-structure grains in the shear zone [32,33]. From the OIM micrographs of the chips which underwent short heat-treatment at various temperatures (Fig. 2 c-e), it is evident that the fraction of unindexed points keeps on decreasing with an increase in the short heat-treatment temperature. This drop in unindexed points indicates the reduction in the fraction of the shear zone with an increase in the short heat-treatment temperature. This might be the result of recovery or recrystallization in the shear zone [34].

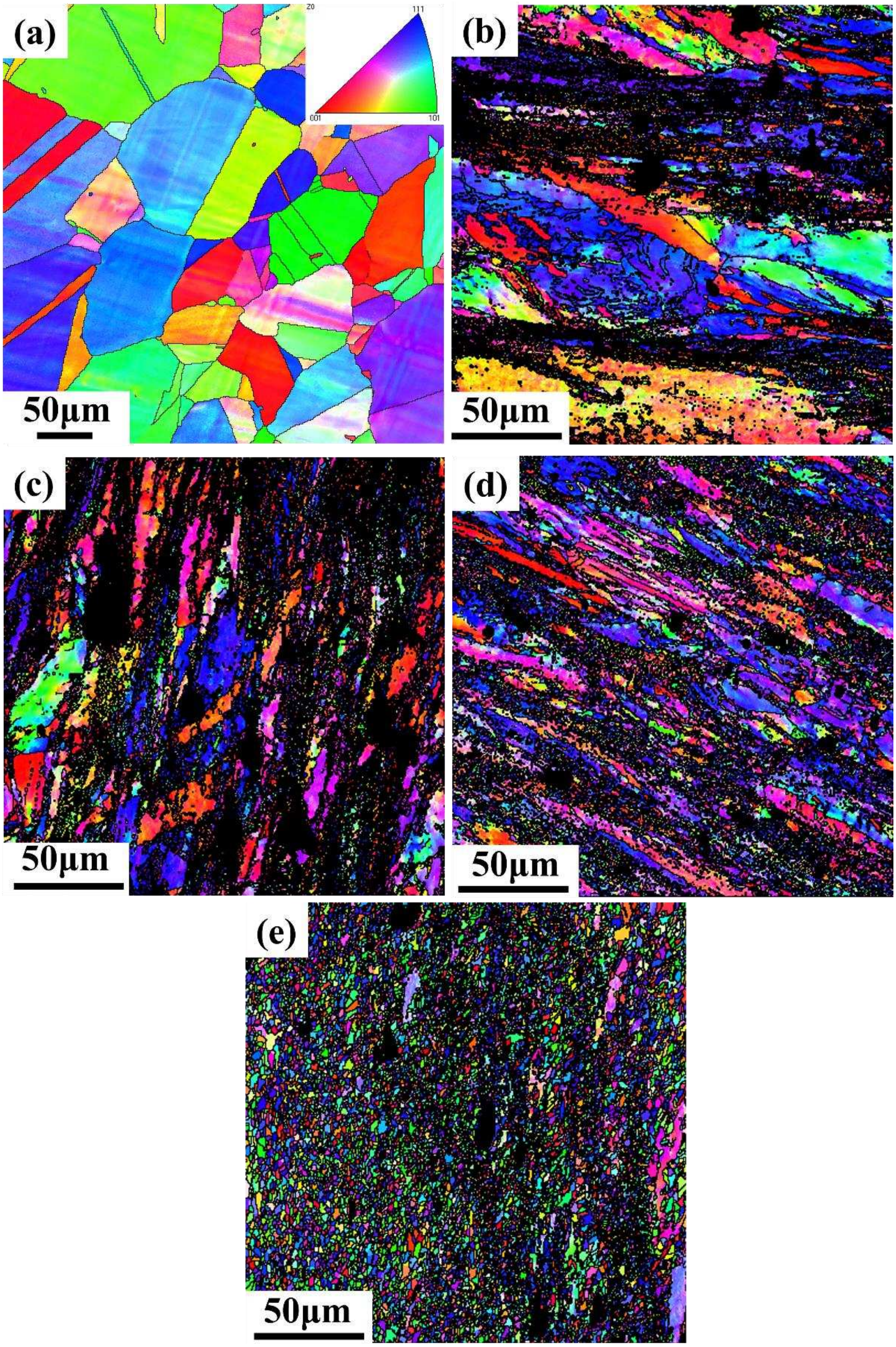

Fig. 2: OIM IPF maps highlighting the presence of equiaxed grains in (a) SA, (b-e) bimodal grain size distribution in (b) AM, (c) SH7, (d) SH8, and (e) SH9 sample, respectively.

### *3.1.2. Transmission electron microscopy*

Though the formation of nanograins during post-deformation heat-treatment was revealed from the OIM micrograph shown in Fig. 2, the limited resolution of EBSD could not truly reveal the nature of nanograins [31,35]. The formation of recrystallized grains with sharp grain boundaries and very fine nano-precipitates that are useful for improving the mechanical and tribological behavior of the material is still unclear from the OIM maps. Transmission electron microscopy (TEM) results can provide a better understanding of the transformations occurring after machining and short heat-treatment of solution annealed IN718 sample. Hence, two samples (AM and SH9 chips) were chosen for TEM analysis as the major microstructural transformation was found to occur only at 900 °C from the OIM analysis, as shown in Fig. 3 and Fig. 4. During short heat-treatments at 700 and 800 °C, partial recrystallization occurred, along with the formation of precipitates.

Bright-field TEM micrographs of AM sample are shown in Fig. 3 (a-c). This figure shows both a large sheared zone and a comparatively less sheared zone, which directly corresponds with the un-indexed zone and moderately refined zone of the respective IPF maps shown in Fig. 2b. Fig. 3a shows the formation of the shear zone, which consists of nanograins and elongated type sub-grain microstructure throughout the sample. Such microstructure is beneficial for improving the wear resistance of materials used in structural applications [36]. An enlarged view of one particular region of Fig. 3a is shown in Fig. 3b, where one can appreciate the formation of very fine grains. The hypothesis can be further confirmed from the selected area diffraction patterns (SADP) of the corresponding micrograph, as shown in Fig. 3c. Approximately continuous ring-type SADP indicates the presence of nanograins. Elongated points in the SADP ring-type pattern also highlight the severity of as-deformed material.

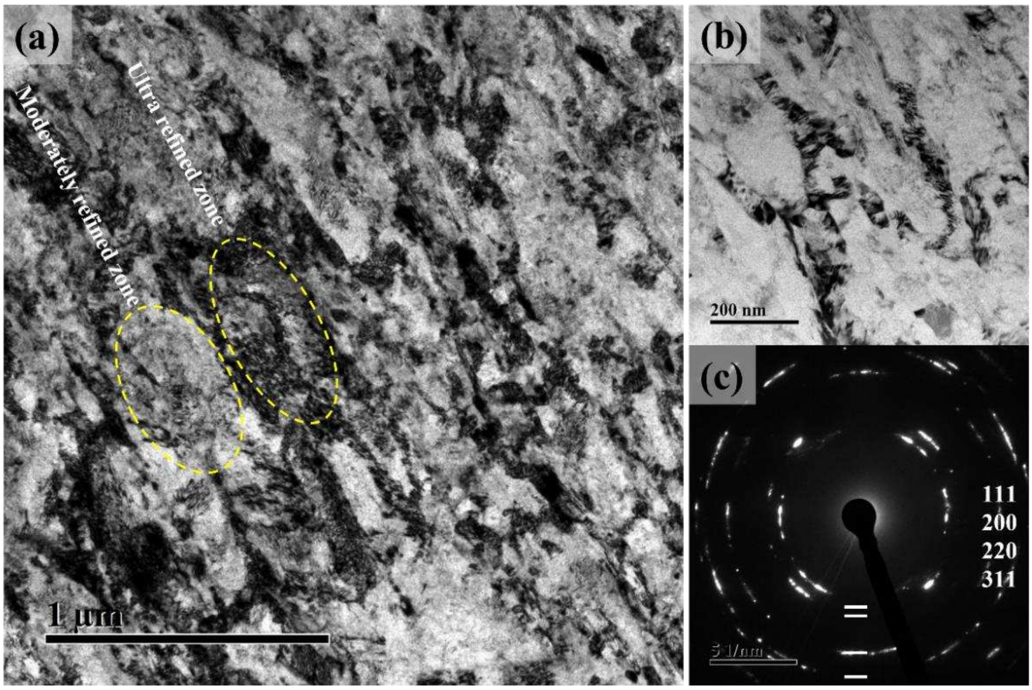

Fig. 3 TEM micrograph (a-b) highlighting the presence of bimodal grain structure in AM sample and (c) its corresponding SADP.

TEM micrographs of SH9 condition shown in Fig. 4 suggest a major change in microstructure in terms of recrystallization. Fig. 4 (a-b) shows the formation of recrystallized grains after thermal treatment along with very fine spherical shape $\gamma^{/}$ nano-precipitates (shown by white arrows) and fine needle shape $\gamma^{//}$ precipitate (shown by red arrows) shown in Fig. 4c. Since the SH9 sample is thermally treated at 900 °C temperature, some of the nano-precipitates grow in size, which can be expected to reduce its mechanical strength (compared to SH7 and SH8 conditions).

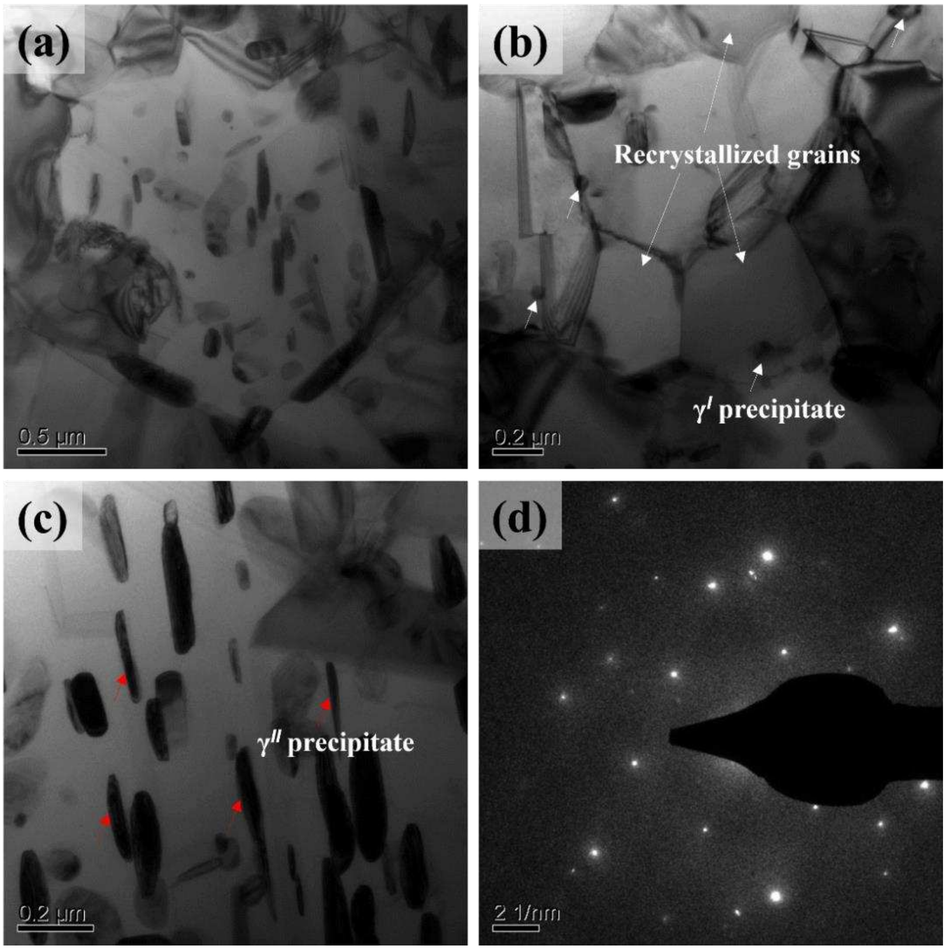

Fig. 4 TEM micrograph (a-c) highlighting the presence of $\gamma'$ precipitate $\gamma''$ precipitate in SH9 sample and (d) its corresponding SADP.

To understand the micro-mechanism of microstructural transformation in AM, SH7, SH8, and SH9 samples, a schematic of the process is shown in Fig. 5. During the machining process, a saturation of dislocation was observed in AM sample, which is shown by a bunch of dislocations. After processing, transformation in microstructure takes place via. transition to subgrain boundaries and grain boundary pinning. The transition of dislocations into subgrain boundaries mainly takes place in AM, SH7, and SH8 samples without much recrystallization because the driving force for recrystallization is quite high in the mentioned sample. Formation of very fine subgrain is shown in AM, SH7, and SH8 samples in Fig. 5, which can be easily correlated with the TEM micrograph of AM sample (Fig. 3).

On the other hand, the generation of nano-precipitates takes place in SH7, SH8, and SH9 samples and causes grain boundary pinning at both low angle and high angle grain boundaries. Formation of low angle boundaries takes place with the help of dislocations, and its pinning by nano-precipitates within the microstructure, as shown by the yellow color dotted circle (Fig. 3a). Subsequently, the pinning of high angle boundary is shown by the red color dotted circle in the TEM micrograph of SH9 sample in Fig. 5. Such a type of grain boundary pinning leads to the thermal stability of processed alloy at elevated temperatures. Eventually, it was also found that such nano-precipitate have been preferentially nucleated at the triple junction (shown by the blue color dotted circle i.e., Fig. 5) and generated triple junction drag in the material, which leads to further enhancement in strength along with strengthening from grain boundary pinning in the processed material.

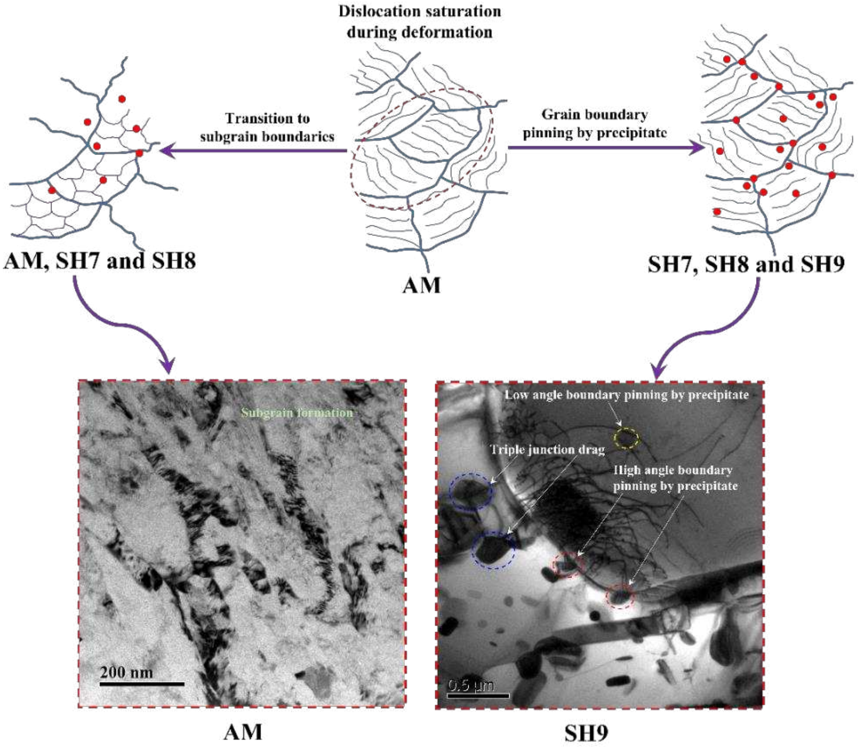

Fig. 5: Schematic highlighting the micro-mechanism of microstructural transformation after machining and subsequent heat-treatment in IN718 alloy.

## 3.2. Mechanical behavior

In order to correlate the effect of post-machining heat-treatment to the wear characteristics, the average hardness value for the different samples is summarized in Fig. 6. It is evident that the average hardness value increases rapidly from 200 to 518 Kgf/mm$^2$ (Fig. 6a), with the deformation induced in the material during machining. This is further reaffirmed from the micrograph shown in Fig. 2b, deformed samples exhibit grains with sizes relatively smaller than in the SA sample. However, the post-machining heat-treatment performed at different temperatures led to the variation in hardness. The sample heat-treated at 700 °C possesses hardness relatively higher than the as-machined sample. Additionally, it is observed that samples heat-treated at further higher temperatures (i.e., 800 °C and 900 °C) show relatively lower hardness values (Fig. 6a). A drop in hardness was observed from 548 Kgf/mm$^2$ (at 700 °C) to 496 Kgf/mm$^2$ (at 800 °C) and further decreased to 364 Kgf/mm$^2$ (at 900 °C). This is attributed to the activation of the static recrystallization from 800 °C followed by complete recrystallization at 900 °C. This recrystallization mechanism results in softening of the materials; thereby, nucleation of new strain-free grains takes place at the expense of highly deforming regions, i.e., region associated saturation of dislocation. Standard deviation associated with the presented hardness values is mentioned in Table 2.

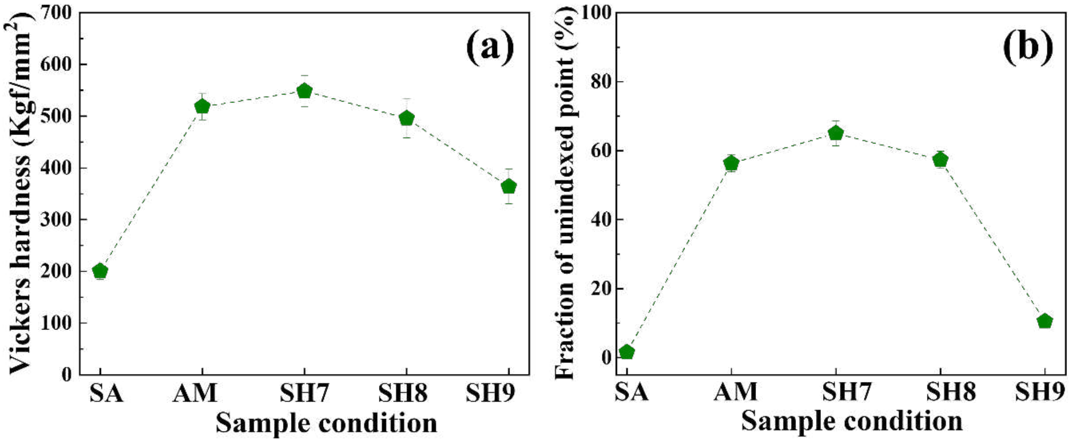

Fig. 6: Variation of (a) Average hardness and (b) Fraction of unindexed point of as-machined and subsequently heat-treated IN718 alloy.

Table 2: Average hardness and fraction of unindexed point after machining and subsequent heat-treatment in IN718 alloy.

| **Sample condition** | **Average hardness ($Kgf/mm^2$)** | **Fraction of unindexed points (%)** |
|---|---|---|
| **SA** | 200.60±8.79 | 1.55±0.72 |
| **AM** | 518.12±25.22 | 56.33±2.52 |
| **SH7** | 548.53±29.56 | 65.0±3.5 |
| **SH8** | 495.86±37.33 | 57.33±2.5 |
| **SH9** | 364.10±33.65 | 10.50±0.71 |

To further strengthen the in-depth understanding of the mechanical behavior of IN718 alloy after machining and subsequent heat-treatment, the fraction of unindexed points are calculated and shown in Fig. 6b. It can be noticed that variation in the Vickers hardness and fraction of unindexed points follows an almost similar trend for all the sample conditions, as observed from Fig. 6 (a-b) and Table 2. The fraction of unindexed points is minimum for SA condition. After machining and short heat-treatement at 700 °C, this fraction can be observed to increase sharply owing to the presence of a large amount of residual strain induced via severe plastic deformation. However, with a further increase in temperature of post-machining heat-treatment, the fraction of unindexed points starts decreasing. The fraction of unindexed points in the short heat-treated samples reduces from ~ 65% at 700 °C (SH7) to ~ 57% at 800 °C (SH8) and ~ 11% at 900 °C (SH9), respectively. The marginal drop in the fraction of unindexed points for SH8 is attributed to recovery taking place in the material, while a substantial drop in SH9 is due to significant recrystallization.

### 3.3. Wear behavior

#### *3.3.1. Wear analysis using scratch test*

During the dry sliding wear test, the variation in the coefficient of friction (COF) with time is recorded, as shown in Fig. 7, and corresponding values are tabulated in Table 3. Within a short span of time, COF values rise drastically; however, soon after that, COF decreases and becomes stable over a period of time. It is evident that steady-state COF values for the SA sample fall over a wide range (~0.001 to ~0.035) ascribed to the presence of severe perturbation, as shown in Fig. 7. However, for the other samples, the COF values lie in the relatively lower range (~0.002 to ~0.019), which suggests that a relatively less amount of wear debris has been generated during the running-in period. As wear debris remain intact in contact with the worn surfaces of the sliding components, three-body wear would be the cause for the evolution of COF along the scratch length.

The evolution of COF is not apparent as its values keep on increasing with the scratch length, which could be probably because of the presence of a large amount of wear debris along with the absence of tribo-film. Also, along with the presence of the wear debris, the existence of tribo-film over the worn surface has a significant influence on the COF and consequently on the wear characteristics. So, it can be understood that the abovesaid two factors might be responsible for the variation in the COF values along the scratch length in the various sample conditions. Also, the presence of tribo-film over the worn surface improves the wear resistance and protects the worn surface from further deterioration. Lower values of COF, i.e., ~0.002 to ~0.012, are observed for the SH7 sample. A better frictional property is obtained after the heat treatment, which must have changed the properties of the contact interface during the scratch test.

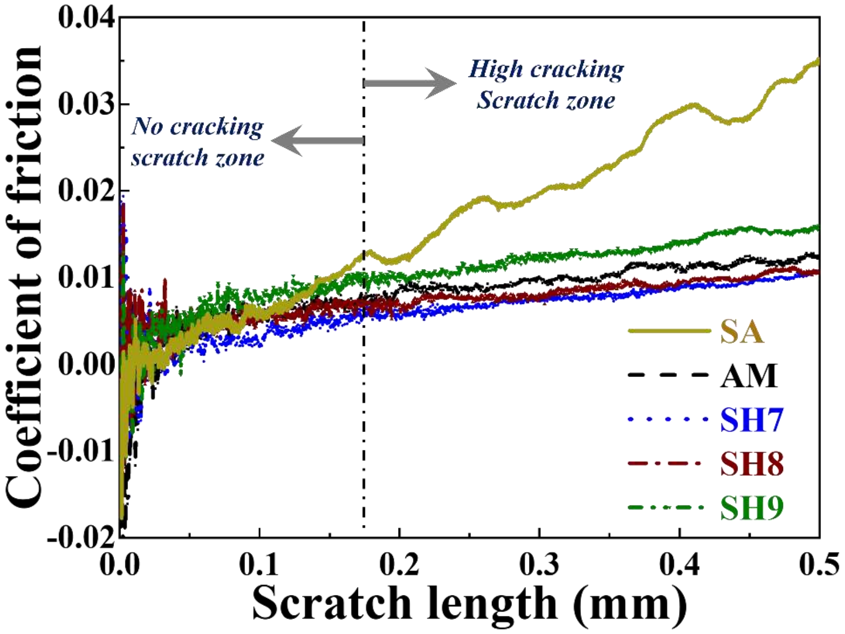

Fig. 7. Variation in coefficient of friction along the scratch length of processed samples.

To corroborate the effect of post-machining heat-treatment on the wear characteristics, i.e., change in wear width (μm), wear depth (μm), and wear volume ($\mu m^3$), various samples were probed using optical profilometry and corresponding 3D-micrographs were captured for the different samples, which are shown in Fig. 8. It is obvious from Fig. 8a and Fig. 8e that sample SA and SH9 exhibit similar characteristics in terms of width and depth of the scar. However, other samples, i.e., AM, SH7, and SH8 exhibit exactly opposite nature compared to that of SA and SH9 samples.

The experimentally obtained wear volume using 3-D optical profilometry was compared with the theoretically measured wear volume, as presented in Table 3. Additionally, the maximum penetration depth (~27.5 μm) and width (~98.44 μm) reported for SA sample can be easily quantified from the color scale bar shown in Fig. 8. Maximum depth and width of penetration in SA sample are attributed to comparatively lower hardness than other samples, i.e., AM, SH7, SH8, SH9, as shown in Figure 6 and Table 2. The average value of penetration depth and width was found to decrease after introducing severe plastic deformation and postprocessing heat-treatment for different samples, i.e., AM, SH7 (i.e., 700 °C), SH8 (i.e., 800 °C), and SH9 (i.e., 900 °C). Among all the samples, SH7 was found to exhibit the lowest penetration depth and width, which results in better wear resistance properties due to the presence of a large fraction of nano-precipitate. These nano-precipitates are majorly responsible for improving the hardness of processed material [37]. The temperature associated with the SH7 sample, i.e., 700 °C is close to the aging temperature of IN718 alloy, which generates a large fraction of nano-precipitate, i.e., $\gamma^{/}$ and $\gamma^{//}$. It results in the pinning of both low and high angle grain boundaries. Among all the samples, SH7 exhibits the best wear resistance and agrees well with the variation of COF, which is shown in Fig. 7.

Table 3: Variation in COF, penetration depth, and width averaged over the scratch length along with experimental and theoretical wear volume.

| **Sample condition** | **COF** | **Penetration depth (µm) at maximum load (mN)** | **Scratch width (µm) at maximum load (mN)** | **Wear volume (×10$^4$ µm$^3$)** | |
|---|---|---|---|---|---|
| | | | | **Experimental** | **Theoretical** |
| **SA** | 0.001-0.035 | 27.5±2.4 | 98.44±1.02 | 5.3±0.24 | 4.73±0.28 |
| **AM** | 0.004-0.017 | 11.6±1.5 | 51.44±1.02 | 0.51±0.17 | 0.85±0.08 |
| **SH7** | 0.002-0.012 | 8.5±0.9 | 46.49±0.23 | 0.40±0.21 | 0.67±0.09 |
| **SH8** | 0.006-0.015 | 11.7±1.3 | 53.49±1.18 | 0.42±0.20 | 0.74±0.07 |
| **SH9** | 0.004-0.019 | 25.6±3 | 60.17±0.7 | 1.26±0.18 | 1.12±0.25 |

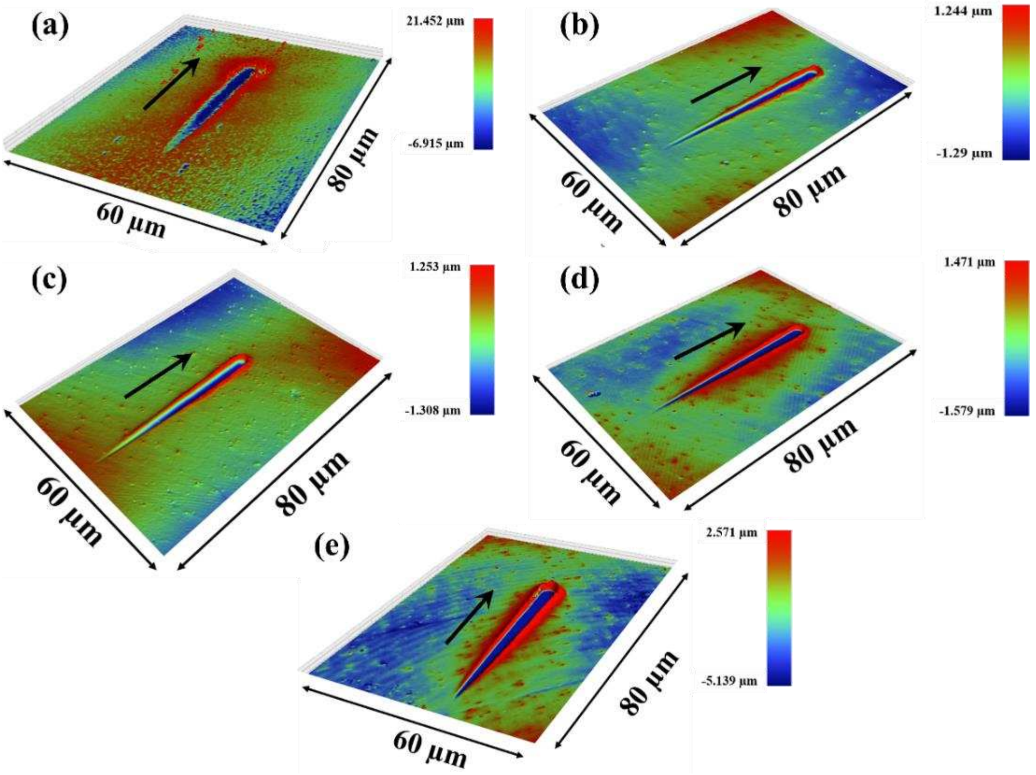

Fig. 8: 3D optical profilometry image of (a) SA, (b) AM, (c) SH7, (d) SH8, and (e) SH9 chips.

Further, it is evident that the penetration depth also varies along the scratch length and follows an increasing trend with an increase in the scratch length except for the SA and SH9 samples, as shown in Fig. 9. Penetration depth for the AM, SH7, and SH8 samples was found to increase linearly, i.e., 11.6 µm, 8.5 µm, and 11.7 µm, respectively, with scratch length increasing to ~0.5 µm. Additionally, some pop-in features (highlighted with orange arrows) are observed for the SA sample (Fig. 9b), indicating that the flow behavior characteristics of the material are discontinuous along the scratch length owing to the formation of small pits and craters during the run-in period. Also, the wear debris gets removed soon after their formation during the wear test; these craters get filled up with the wear debris and consequently result in exceptional wear characteristics with pop-in features. Additionally, typical symmetrical pile-up type characteristics can also be seen all along the length near the edges of the scratch, similar to the material's response during indentation [29], as shown in Fig. 9a. In agreement with the previous results, the sample post-process heat-treated at 700 °C showed minimum pile-up at the edges of the scratch. Thus, the heat treatment temperature after the machining operation influences the wear depth along the scratch length.

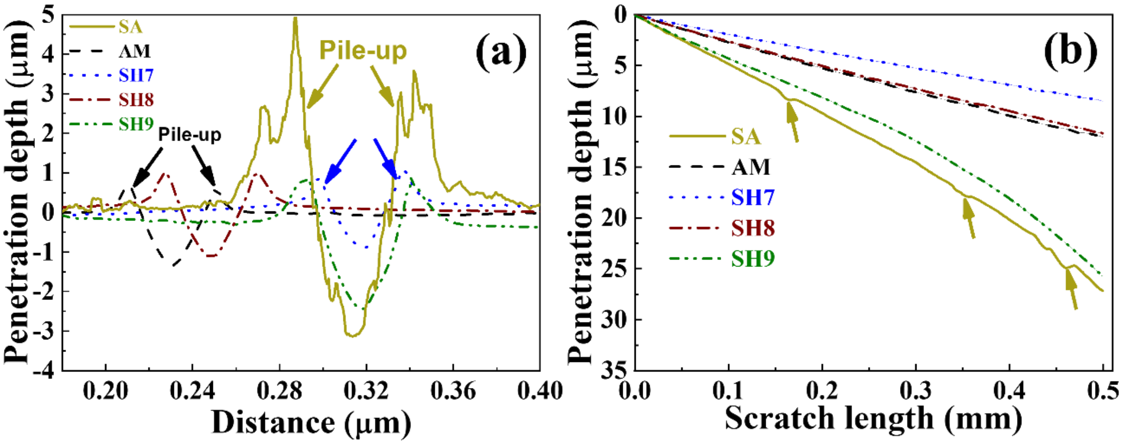

Fig. 9: Variation of (a) maximum penetration depth of scratch along the width of the scratch and (b) penetration depth along the length of the scratch.

Further, to dig deep into the wear behavior of the materials during the scratch test and understand the wear mechanism, variation in the frictional force ($F_T$) with the normal force ($F_N$) is presented in Fig. 10. There are some apparent fluctuations in the $F_T$ during the test owing to the presence of wear debris in the contact interface shown in Fig. 12. The magnitude of friction force corresponding to the SH7 sample remains lower than that for the other sample conditions at all levels of normal force (0 to 5 N). This is attributed to the relatively high hardness of the SH7 in comparison to the hardness of the other samples (Table 2). Additionally, during the initial stages (<1 N load), various friction force profiles corresponding to different samples are very closely spaced, ascribed to the gradual wear of the material without any sign of craters and the formation of a cracking zone [38]. However, beyond an applied normal force of 1 N, the spacing between the frictional profiles decreases continuously with the increasing magnitude of the normal force. At all the load levels

(>2.5 N), fluctuations can be seen all along the friction force profiles due to failure of the materials via flaking, formation of the crater, and cracks along the scratch length.

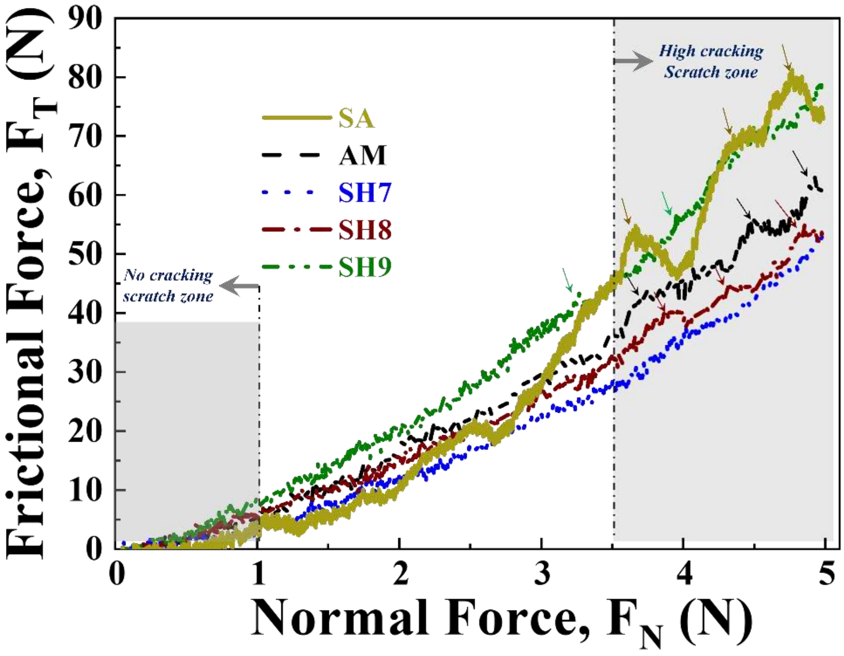

Fig. 10: Variation of frictional force and normal force in as-machined and subsequently heat-treated IN718 alloy.

### 3.3.2. Investigation of wear volume

To further comprehend the overall effect of machining and post-machining heat-treatment on the wear damage, wear volume was estimated using Eq. 1-2. Fig. 11a presents a good comparison between the experimentally obtained and theoretically estimated wear measurements. It can be observed that the experimentally calculated wear volume decreases drastically from $5.3\times10^4$ to $0.51\times10^4$ $\mu m^3$ with the severe plastic deformation followed by subsequent heat-treatment. In corroboration with the penetration depth variation (Fig. 11b), the wear volume further decreases to $0.4\times10^4$ $\mu m^3$ for SH7. After that, wear volume followed the increasing trend and increased to $1.26\times10^4$ $\mu m^3$ for SH9. Also, experimentally measured wear volume values follow the same trend, similar to the variation of penetration depth along the scratch length, as described in Fig. 8 and Fig. 9. The wear volume for the SA is relatively higher than other sample conditions, and these results are in good agreement with the COF values shown in Table 3. Moreover, the specific wear rate was also estimated using Eq. 3, and is shown in Fig. 11c, which follows a similar trend as that of wear volume reported for different samples. Subsequently, marginal difference in wear rate values (Fig. 11c) obtained from optical profilometry and theoretical calculation attribute to variation in COF values along the scratch length, as shown in Fig. 7.

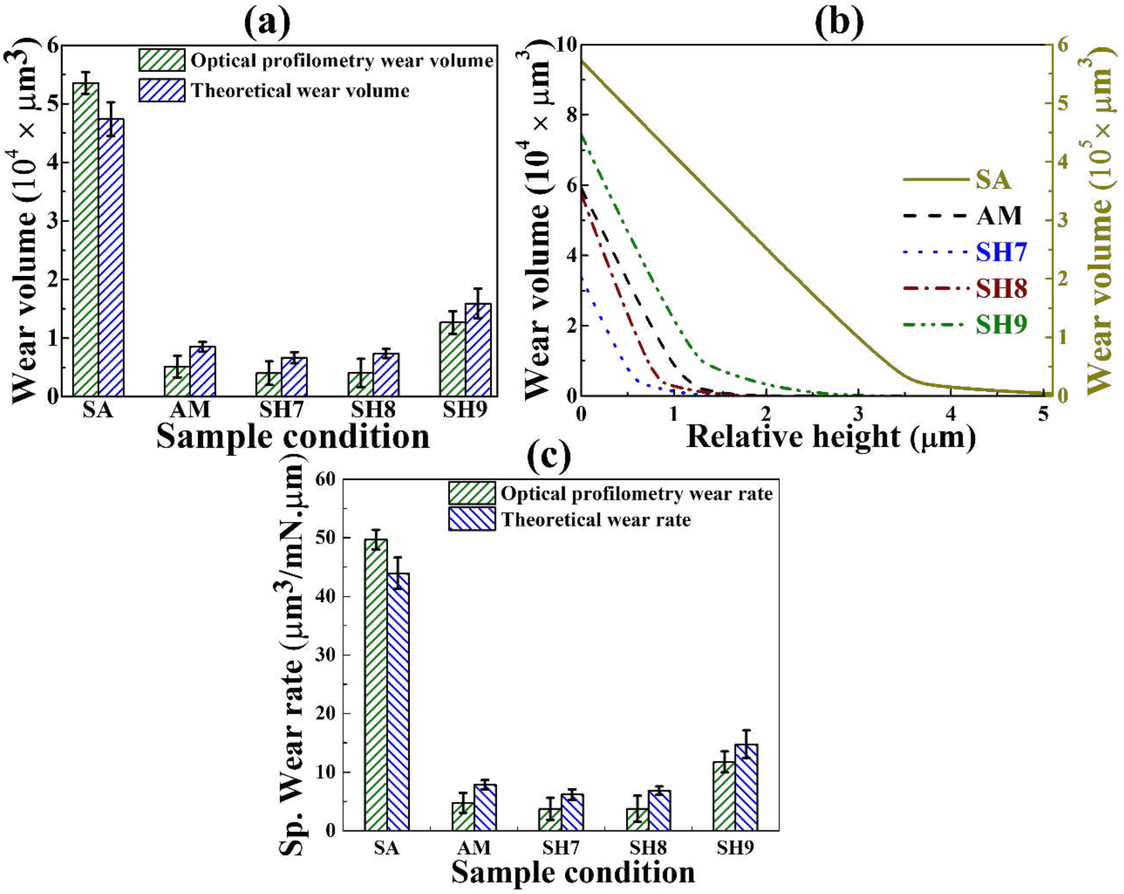

Fig. 11: (a) Quantitative comparison between experimentally and theoretically obtained wear volume, (b) Variation of wear volume with a relative height of the scar, and (c) wear rate of different sample conditions.

### *3.3.3. Worn surface analysis*

Further, to investigate the fracture behavior of the worn surfaces in the scratch samples, fractography analysis was carried out. Fig. 12 shows the SEM micrograph of worn surface of different samples processed through machining and subsequent heat-treatments. A comparatively smoother region throughout the AM chip indicates minimal wear (Fig. 12a), which is also confirmed by the worn surface height of AM sample. Another reason behind the lesser wear of this chip is increased Vickers hardness. For in-depth investigation, a higher magnification image was also captured at the center and periphery of the scratch, as shown in Fig. 12 a1 and a2, respectively. Regions a1 and a2 together show that severe fracture occurs at the periphery of scratch along with nominal fracture at the center during the plastic flow of material throughout the scratch test. After introducing thermal treatment at 700 $^{o}$C, the worn surface of SH7 was found to be similar to that of AM sample, except the periphery of the scratch, which is shown in Fig. 12 (b-b2). Further increase in heat-treatment temperature up to 800 $^{o}$C leads to the introduction of fracture in the central region of scratch along with the periphery in terms of micro-cracks during the plastic flow of material (Fig. 12 c-c2).

From AM to SH8 sample, the fracture mode of thermally treated sample was found to be almost similar, with a marginal change in SH8 condition. Microstructural evolution and mechanical results mentioned above support the worn surface morphology of the different samples. However, a drastic change in the mode of fracture was observed in the SH9 sample. Fig. 12 (d-d2) shows the worn surface of the SH9 sample consisting of a large fraction of micro-cracks (shown by black arrows) along with fine abrasive particles embedded in the material (shown by red arrow) in the central region of the scratch. These micro-cracks have formed during the severe plastic deformation in the zone beneath the worn surface along the scratch length. This is mainly attributed to the increase in the dislocation density within these regions during the wear test itself, which later lead to the initiation and propagation of cracks in the sub-surface regions. Similar observations have also been reported in the literature [29,39]. Central crack was found to be wide and deeper in nature, which is clearly shown in Fig. 12 d1. Along with wider crack, some region shows adhesive wear, as shown by the black dotted ellipse, which eventually turns out to be crater wear. After careful observation, we found that the size of the crack along the periphery of the scratch increased significantly along with the accumulation of materials (Fig. 12 d2). This combined effect indicates the severity of deformation in the SH9 sample during plastic flow. The presence of a deep crater, embedded abrasive particle, and wider crack indicate that SH9 sample is the least wear-resistant among all the processed conditions.

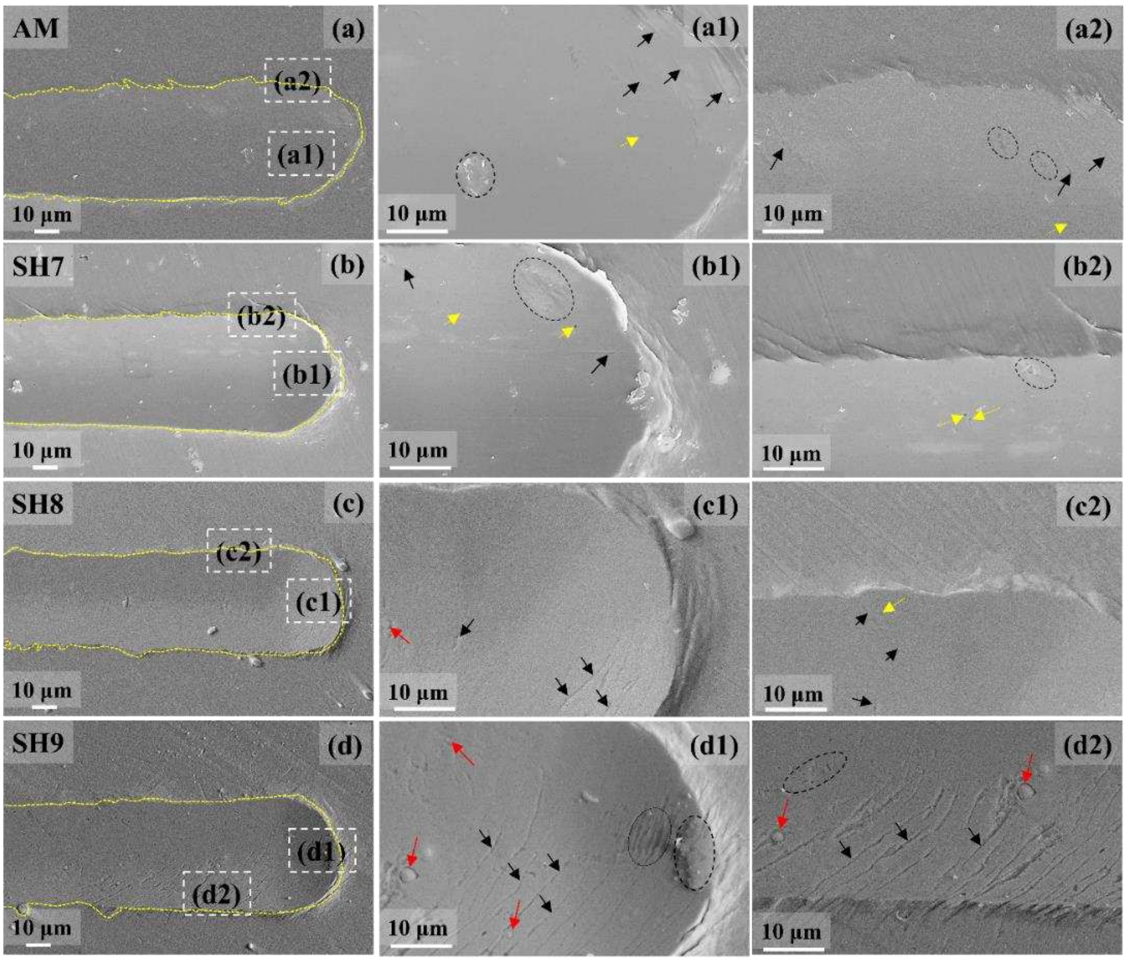

Fig. 12: (a-d) Secondary electron (SE) micrograph of the worn surfaces obtained nearby the tip of the scratch along with various features highlighted in (a1-d1) inside the surface and (a2-d2) at the periphery of the scratch.

### *3.3.4. Acoustic emission*

Acoustic emission is the phenomenon of the transmission of the elastic or acoustic wave in solid material when it changes its internal structure during the highly irreversible severe plastic deformation process [40], which is plane strain machining in the current study. Severe plastic deformation leads to the generation of localized sources of elastic or acoustic waves.

In most severe deformation processes, acoustic emission is found to be an instrumental technique to detect, locate, and characterize the damage [41,42]. Therefore, to characterize the damage that occurred during the scratch test of processed material, acoustic emission was investigated, and the data obtained are plotted in Fig. 13. This figure shows a series of broader peaks (shown by orange color arrows) for SA sample of larger amplitude, which reflects the generation of propagation of micro-cracks. However, AM sample shows quite a smooth region (without the formation of any micro-cracks) throughout the scratch length. Also, in SH7 sample, a considerable alteration in the smoothness was not observed. Peaks of comparatively higher amplitude were observed with a further increase in heat-treatment temperature, which attributed to the onset of formation of a large fraction of micro-cracks for SH8 and SH9 samples. The formation of such micro-crack is clearly shown in the SEM image in Fig. 12 c and Fig. 12 d. With progress in the scratch test, the size of generated micro-crack increased, and worn particles obtained during the test got arrested in the vicinity of large cracks, as shown in Fig. 12 d. Although the frequency and amplitude of generation and transmission of such micro-cracks are comparatively lower in samples other than the SA sample, they still exist on the friction surface up to the SH9 sample.

Eventually, an interesting observation was noticed during plastic deformation in terms of non-uniform transmission of elastic waves whose crests are quasiperiodic (or irregular periodic) in the form of generated waves, and the crest is found to be perpendicular to the friction direction. Therefore, one can say unequivocally that acoustic emission can be used as a tool to investigate the transmission of the acoustic wave from elastic to intense plastic deformation, which results in a continuous drop in the frequency of oscillating wave produced in the tribological system.

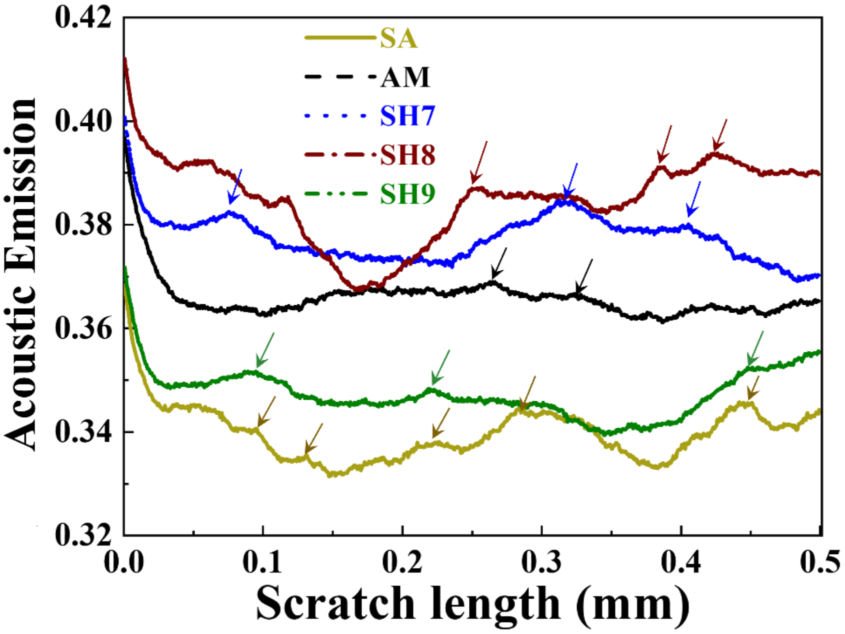

Fig. 13: Variation of acoustic emission of as-machined and subsequently heat-treated IN718 alloy.

## 4. Conclusions

After performing the scratch test of plane strain machined and thermally treated IN718 superalloy, the following pertinent conclusions were drawn:

- The bimodal microstructure obtained in plane strain machining was consistent up to SH8 condition.
- Average hardness and noise fraction of processed samples show that material retained its high strength up to SH7 sample, followed by a drop in its values.
- Significant perturbation in COF variation along the scratch length of SA sample leads to continuous fracture of the material. Eventually, this variation was found to be marginal for other samples, indicating the improvement in wear resistance.
- Wear resistance of the SH7 sample was found to be maximum due to precipitate pining. In contrast, the marginal drop in value was obtained for SH8 sample due to

precipitate coarsening and then a large drop for SH9 due to an increase in recrystallization.

- Continuous shearing of material along with the generation of micro-cracks takes place up to SH8, whereas generation of macro-crack followed by fine particle abrasion takes place in SH9 sample.

Based on the aforementioned results, we conclude that as-deformed material followed by thermal treatment up to 700 °C is the most wear-resistant nano-grained material as precipitate pinning and eventually retarded recrystallization is most impactful at this temperature. At higher temperature heat treatment, the wear resistance degrades; still, it is significantly better than that of SA conditon. The primary cause behind such degradation in property is precipitate coarsening and an increase in recrystallization.

## CRediT authorship contribution statement

**Prabhat Chand Yadav:** Conceptualization, Methodology, Investigation, Software, Validation, Formal analysis, Writing-Original Draft, Writing - Review & Editing. **Prince Setia**: Investigation, Formal analysis, Software, Data curation, Writing-Original Draft, Writing - Review & Editing. **Sandeep Sahu**: Investigation, Formal analysis, Writing - Original Draft, Writing - Review & Editing.

## Declaration of Competing Interest

The authors declare that they have no known competing financial interests or personal relationships that could have appeared to influence the work reported in this paper.

## Acknowledgment

PCY acknowledges the support from Advanced Center for Materials Science (ACMS), IIT Kanpur, for conducting EBSD and scratch tests. SS is thankful to the Royal Society for providing Newton International Fellowship NIF\R1\201789. The authors also acknowledge

Dr. Bhagyaraj Jayabalan at IIT Kanpur for providing a TEM sample preparation facility and fruitful discussion on TEM results.

## References

1. Y.-T. Chen, A.-C. Yeh, M.-Y. Li, S.-M. Kuo, Effects of processing routes on room temperature tensile strength and elongation for Inconel 718, Mater. Des. 119 (2017) 235-243, https://doi.org/10.1016/j.matdes.2017.01.069.
2. B. Geddes, H. Leon, X. Huang, Superalloys: alloying and performance. ASM International: 2010
3. P.C. Yadav, S. Sahu, A. Subramaniam, S. Shekhar, Effect of heat-treatment on microstructural evolution and mechanical behavior of severely deformed Inconel 718, Mater. Sci. Eng. A 715 (2018) 295-306, https://doi.org/10.1016/j.msea.2018.01.007.
4. S.A. Nalawade, M. Sundararaman, J.B. Singh, A. Verma, R. Kishore, Precipitation of γ′ phase in δ-precipitated Alloy 718 during deformation at elevated temperatures, Mater. Sci. Eng. A 527 (2010) 2906-2909, https://doi.org/10.1016/j.msea.2010.01.006.
5. J.K. Tien, G.E. Vignoul, M.W. Kopp, Materials for elevated-temperature applications, Mater. Sci. Eng. A 143 (1991) 43-49, https://doi.org/10.1016/0921-5093(91)90724-2.
6. Y. Liu, Q. Guo, C. Li, Y. Mei, X. Zhou, Y. Huang, H. Li, Recent progress on evolution of precipi-tates in inconel 718 superalloy, Acta Metall. Sin. 52 (2016) 1259-1266, https://doi.org/10.11900/0412.1961.2016.00290.
7. M. Godec, S. Malej, D. Feizpour, Č. Donik, M. Balažic, D. Klobčar, L. Pambaguian, M. Conradi, A. Kocijan, Hybrid additive manufacturing of Inconel 718 for future space applications, Mater. Charact. 172 (2021) 110842, https://doi.org/10.1016/j.matchar.2020.110842.
8. F. Soffel, D. Eisenbarth, E. Hosseini, K. Wegener, Interface strength and mechanical properties of Inconel 718 processed sequentially by casting, milling, and direct metal deposition, J. Mater. Process. Technol. 291 (2021) 117021, https://doi.org/10.1016/j.jmatprotec.2020.117021.
9. A.R.C. Sharman, J.I. Hughes, K. Ridgway, Workpiece Surface Integrity and Tool Life Issues When Turning Inconel 718™ Nickel Based Superalloy, Mach. Sci. Technol. 8 (2004) 399-414, https://doi.org/10.1081/MST-200039865.
10. R.S. Pawade, S.S. Joshi, P.K. Brahmankar, Effect of machining parameters and cutting edge geometry on surface integrity of high-speed turned Inconel 718, Int. J. Mach. Tools Manuf. 48 (2008) 15-28, https://doi.org/10.1016/j.ijmachtools.2007.08.004.
11. P.K. Wright, J.G. Chow, Deformation Characteristics of Nickel Alloys During Machining, J. Eng. Mater. Technol. 104 (1982) 85-93, https://doi.org/10.1115/1.3225057.
12. A. Houghton, R. Lewis, U. Olofsson, J. Sundh, Characterising and reducing seizure wear of inconel and incoloy superalloys in a sliding contact, Wear 271 (2011) 1671-1680, https://doi.org/10.1016/j.wear.2011.02.022.
13. S. Ramesh, G. Anne, H.S. Nayaka, S. Sahu, M.R. Ramesh, Investigation of dry sliding wear properties of multi-directional forged Mg–Zn alloys, J. Magnes. Alloy. 7 (2019) 444-455, https://doi.org/10.1016/j.jma.2019.05.008.

14. A. Thakur, S. Gangopadhyay, State-of-the-art in surface integrity in machining of nickel-based super alloys, Int. J. Mach. Tools Manuf. 100 (2016) 25-54, https://doi.org/10.1016/j.ijmachtools.2015.10.001.
15. X.-P. Ren, Z.-Q. Liu, Microstructure refinement and work hardening in a machined surface layer induced by turning Inconel 718 super alloy, Int. J. Miner. Metall. 25 (2018) 937-949, https://doi.org/10.1007/s12613-018-1643-2.
16. Z. Liao, D. Axinte, M. Mieszala, R. M'saoubi, J. Michler, M. Hardy, On the influence of gamma prime upon machining of advanced nickel based superalloy, CIRP Annals 67 (2018) 109-112, https://doi.org/10.1016/j.cirp.2018.03.021.
17. Z. Liao, M. Polyakov, O.G. Diaz, D. Axinte, G. Mohanty, X. Maeder, J. Michler, M. Hardy, Grain refinement mechanism of nickel-based superalloy by severe plastic deformation - Mechanical machining case, Acta Mater. 180 (2019) 2-14, https://doi.org/10.1016/j.actamat.2019.08.059.
18. K. Zhuang, D. Zhu, X. Zhang, H. Ding, Notch wear prediction model in turning of Inconel 718 with ceramic tools considering the influence of work hardened layer, Wear 313 (2014) 63-74, https://doi.org/10.1016/j.wear.2014.02.007.
19. H. Touazine, M. Jahazi, P. Bocher, Influence of Hard Turning on Microstructure Evolution in the Subsurface Layers of Inconel 718. In ASME 2014 International Mechanical Engineering Congress and Exposition, Montreal, QC, Canada, (2014), Vol. Volume 2A: Advanced Manufacturing
20. E.O. Ezugwu, Z.M. Wang, C.I. Okeke, Tool Life and Surface Integrity When Machining Inconel 718 With PVD- and CVD-Coated Tools, Tribol. Trans. 42 (1999) 353-360, https://doi.org/10.1080/10402009908982228.
21. D.G. Thakur, B. Ramamoorthy, L. Vijayaraghavan, Effect of cutting parameters on the degree of work hardening and tool life during high-speed machining of Inconel 718, Int. J. Adv. Manuf. Technol. 59 (2012) 483-489, https://doi.org/10.1007/s00170-011-3529-6.
22. X. Ren, Z. Liu, Influence of cutting parameters on work hardening behavior of surface layer during turning superalloy Inconel 718, Int. J. Adv. Manuf. Technol. 86 (2016) 2319-2327, https://doi.org/10.1007/s00170-016-8350-9.
23. S. Rinaldi, S. Imbrogno, G. Rotella, D. Umbrello, L. Filice, Physics based modeling of machining Inconel 718 to predict surface integrity modification, Procedia CIRP 82 (2019) 350-355, https://doi.org/10.1016/j.procir.2019.04.150.
24. J. Zhou, V. Bushlya, P. Avdovic, J.E. Ståhl, Study of surface quality in high speed turning of Inconel 718 with uncoated and coated CBN tools, Int. J. Adv. Manuf. Technol. 58 (2012) 141-151, https://doi.org/10.1007/s00170-011-3374-7.
25. A. Devillez, G. Le Coz, S. Dominiak, D. Dudzinski, Dry machining of Inconel 718, workpiece surface integrity, J. Mater. Process. Technol. 211 (2011) 1590-1598, https://doi.org/10.1016/j.jmatprotec.2011.04.011.
26. M.E. Merchant, Mechanics of the metal cutting process. I. Orthogonal cutting and a type 2 chip, J. Appl. Phys. 16 (1945) 267-275, https://doi.org/10.1063/1.1707586.
27. C. Milton, M. Shaw, Metal cutting principles. Clarendon Press, Oxford Science Publication, UK (1984)

28. A. Nisar, K. Balani, Role of Interfaces on Multi-length Scale Wear Mechanics of TaC-based Composites Adv. Eng. Mater. 19 (2017) 1600713, https://doi.org/10.1002/adem.201600713.
29. P. Setia, K. Vishwanath, K. Mondal, T. Venkateswaran, S.S. Singh, S. Shekhar, Cushioning effect of austenite in silicon stainless steels (SiSS) leading to improved wear resistance, Tribol. Int. 173 (2022) 107678, https://doi.org/10.1016/j.triboint.2022.107678.
30. J.F. Archard, Contact and Rubbing of Flat Surfaces, J. Appl. Phys. 24 (1953) 981-988, https://doi.org/10.1063/1.1721448.
31. S. Shekhar, N.K. Sharma, S. Sahu, S. Misra, Electron Backscatter Diffraction Technique: Fundamentals to Applications. In Electron Microscopy in Science and Engineering, K. Biswas, S. Sri, N. Gurao (eds.), Springer Nature, Singapore, (2022), pp 35-60
32. M. Ravi Shankar, R. Verma, B.C. Rao, S. Chandrasekar, W.D. Compton, A.H. King, K.P. Trumble, Severe Plastic Deformation of Difficult-to-Deform Materials at Near-Ambient Temperatures, Metall. Mater. Trans. A 38 (2007) 1899-1905, http://dx.doi.org/10.1007/s11661-007-9257-8.
33. M. Ravi Shankar, B.C. Rao, S. Chandrasekar, W. Dale Compton, A.H. King, Thermally stable nanostructured materials from severe plastic deformation of precipitation-treatable Ni-based alloys, Scr. Mater. 58 (2008) 675-678, http://dx.doi.org/10.1016/j.scriptamat.2007.11.040.
34. F. Humphreys, M. Hatherly, Recrystallization and Related Annealing Phenomena. Elsevier, Oxford: 2004
35. S. Sahu, P.C. Yadav, S. Shekhar, Use of Hot Rolling for Generating Low Deviation Twins and a Disconnected Random Boundary Network in Inconel 600 Alloy, Metall. Mater. Trans. A 49 (2018) 628-643, https://doi.org/10.1007/s11661-017-4431-0.
36. R. Sahoo, B. Jha, T. Sahoo, Dry sliding wear behavior of Ti–6Al–4V alloy consisting of bimodal microstructure, Trans. Indian Inst. Met. 67 (2014) 239-245, https://doi.org/10.1007/s12666-013-0343-x.
37. M.C. Chaturvedi, Y.-F. Han, Strengthening mechanisms in Inconel 718 superalloy, Met. Sci. 17 (1983) 145-149, https://doi.org/10.1179/030634583790421032.
38. A. S, R. Maurya, Assessment of plasma sprayed carbon nanotube reinforced Al2O3-based nanocomposite with micro-scratching, Surf. Coat. Technol. 418 (2021) 127216, https://doi.org/10.1016/j.surfcoat.2021.127216.
39. N.P. Suh, The delamination theory of wear, Wear 25 (1973) 111-124, https://doi.org/10.1016/0043-1648(73)90125-7.
40. S.J. Vahaviolos, Acoustic emission: standards and technology update. ASTM USA(1999)
41. M.J. Eaton, R. Pullin, K.M. Holford, Acoustic emission source location in composite materials using Delta T Mapping, Compos. - A: Appl. Sci. Manuf. 43 (2012) 856-863, https://doi.org/10.1016/j.compositesa.2012.01.023.
42. J.P. Mccrory, S.K. Al-Jumaili, D. Crivelli, M.R. Pearson, M.J. Eaton, C.A. Featherston, M. Guagliano, K.M. Holford, R. Pullin, Damage classification in carbon fibre composites using acoustic emission: A comparison of three techniques, Compos. B. Eng. 68 (2015) 424-430, https://doi.org/10.1016/j.compositesb.2014.08.046.